applied optics

Development and application of an airborne differential absorption lidar for the simultaneous measurement of ozone and water vapor profiles in the tropopause region

Andreas Fix,[1,*] Felix Steinebach,[1,2] Martin Wirth,[1] Andreas Schäfler,[1] and Gerhard Ehret[1]

[1]Deutsches Zentrum für Luft- und Raumfahrt (DLR), Institut für Physik der Atmosphäre, 82234 Oberpfaffenhofen, Germany
[2]Current address: TWK-ELEKTRONIK GmbH, Heinrichstrasse 85, 40239 Düsseldorf, Germany
*Corresponding author: andreas.fix@dlr.de

Received 29 April 2019; revised 17 June 2019; accepted 17 June 2019; posted 18 June 2019 (Doc. ID 366225); published 22 July 2019

A new, combined, lidar system has been developed that is able to simultaneously measure profiles of ozone and water vapor onboard aircraft. The concurrent measurement of these complementary trace species in the upper troposphere and lower stratosphere allows inferring exchange processes in the tropopause region. Whereas an advanced H_2O differential absorption lidar at 935 nm has successfully been developed and extensively tested at DLR in the past, we describe here an amendment of this lidar by the addition of an ultraviolet (UV) channel to measure ozone. The transmitter of the ozone differential absorption lidar (DIAL) is based on a near-IR optical parametric oscillator that is frequency-converted into the UV spectral range by intracavity sum frequency mixing. Hereby, a continuous UV tuning range of ~297–317 nm has been achieved. The average output power in this range is higher than 1 W corresponding to more than 10 mJ per pulse at a repetition rate of 100 Hz. The ozone DIAL system has been carefully characterized both on the ground and in flight. The first simultaneously measured two-dimensional cross-sections of ozone and water vapor in the upper troposphere and lower stratosphere have been recorded during the Wave-driven Isentropic Exchange (WISE) field campaign in 2017 demonstrating the high potential of this system for studying exchange processes in this region of the atmosphere.

https://doi.org/10.1364/AO.58.005892

1. INTRODUCTION

Stratosphere-troposphere exchange (STE) is a key controlling factor for the ozone budget in the upper troposphere (UT) and water vapor variability in the lower stratosphere (LS). The water vapor and ozone flux across the tropopause has a large impact on atmospheric chemistry and the Earth's radiation budget and thus, the understanding of the relevant processes is important for our ability to predict climate change [1].

Despite their importance, these transport processes and their contribution to the constituent distribution in the UTLS are still inadequately understood. Difficulties remain in estimating the magnitude of STE, and large uncertainties exist in the geographic distributions, seasonality, and long-term changes of STE. There is some evidence that both the acceleration of the Brewer-Dobson circulation and stratospheric ozone recovery will tend to increase the future global tropospheric ozone burden through enhanced STE [2].

Therefore, more measurements in the tropopause region are required to assess the dynamical, chemical and radiative coupling between stratosphere and troposphere.

In general, a commonly used technique to investigate mixing between stratosphere and troposphere is tracer correlation. Aircraft *in situ* measurements have provided insight into these processes by correlating trace species that strongly contrast in their stratospheric and tropospheric abundance such as ozone and carbon monoxide (e.g., [3–6]).

Ozone and water vapor are considered to be complementary tracers since stratosphere and troposphere show significant contrast in the mixing ratios of ozone (high in the former, and low in the latter) and water vapor (low in the former, and high in the latter) [7].

Simultaneous lidar measurement of O_3 and H_2O profiles in the tropopause region with high accuracy and high spatial resolution would therefore constitute a major step forward helping to assess STE using tracer correlation (Fig. 1). From the ground, it is difficult to measure UT water vapor [8,9], however, ozone lidars operating in the ultraviolet (UV) spectral range have been employed for STE investigations [9–12]. An autonomous system combining the differential absorption lidar (DIAL) technique (for O_3) and Raman lidar (for H_2O) has

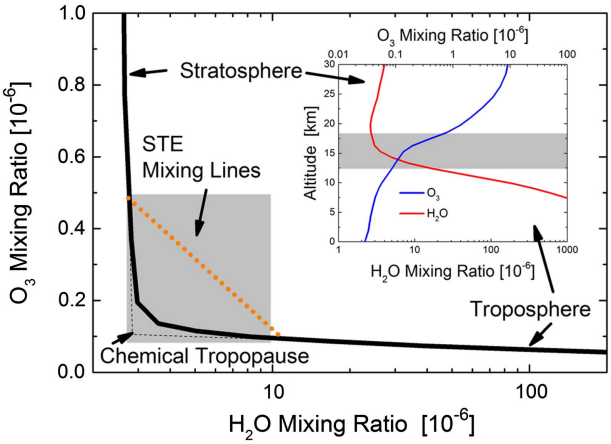

Fig. 1. Conceptual depiction of water vapor to ozone correlation in the tropopause region. Both tracers show opposite behavior (see inset) since stratosphere and troposphere exhibit significant contrast in abundance of ozone (high in the former, and low in the latter) and water vapor (vice versa). The mixing ratio of these tracers exhibits a strong gradient across the tropopause because it acts as a transport barrier. In tracer space an L-shaped correlation is derived from these profiles (black line). When mixing occurs, the correlation will deviate from the L-shaped correlation, and the resulting "mixing lines" thus feature intermediate chemical characteristics and thus are an indication of STE.

been developed, but requires averaging times on the order of 10–30 min and provides water vapor profiles in the lower atmosphere and only during nighttime [13]. Airborne *in situ* measurements can only provide one-dimensional data along flight trajectories. In general, satellite measurements from e.g., limb sounders [14,15] can provide simultaneous measurements of those tracers, but in the tropopause region their resolution does not fall below 1 km in the vertical and ∼100 km in the horizontal. Therefore, they have difficulties in resolving the length scales of the features responsible for STE. It is also important that viewing geometries and averaging kernels are comparable for both tracers. Nevertheless, climatological analyses of H_2O/O_3 tracer correlations from satellites were derived and gainfully used [14,15].

Thus, airborne DIAL measurements of ozone and water vapor appear very promising, since two-dimensional cross-sections of their concentrations with high vertical and horizontal resolution can provide instantaneous information on the horizontal and vertical structure of ozone and water vapor, and deduced tracer correlations can contribute to an improved assessment of STE in the UT and LS.

In order to meet this goal, the water vapor and aerosol lidar system (WALES) that has been developed at DLR was upgraded by means of an additional ozone measuring capability. Due to the wavelength range used (at 935 nm), WALES is currently the only airborne H_2O DIAL capable of measuring UTLS water vapor with adequate precision [16] and also features High Spectral Resolution lidar (HSRL) capability at 532 nm. This system was designed to fly on the German research aircraft HALO, a Gulfstream G550 [17], and was deployed within numerous airborne campaigns [18–32]. As pointed out [28,33], aerosol is a very good additional tracer for STE. An airborne lidar system capable of measuring all three species (water vapor, aerosol, and ozone) therefore constitutes a very powerful instrument.

In the subsequent sections, the spectral requirements for UV-DIAL will be briefly reviewed followed by the description of the experimental set-up, a detailed characterization of the system's performance in the lab, and its first successful employment for ozone measurements both on ground and in flight which illustrates its capabilities. Finally, the first two-dimensional simultaneous measurements of ozone and water vapor in the mid-latitude tropopause region are presented.

2. REQUIREMENTS

In its original version, the WALES lidar system [16] consists of two identical, homebuilt laser systems (see Table 1) that both comprise a near-infrared (NIR) frequency converter pumped by a diode-pumped Nd:YAG laser at a repetition rate of 100 Hz. Each transmitter sequentially generates two of the four wavelengths in the vicinity of 935 nm to measure water vapor from the boundary layer to the lower stratosphere. The NIR frequency converters are based on optical parametric oscillators (OPOs) and are attached as front-end modules to the pump lasers (see Fig. 2). This system has been successfully operated during many flight campaigns on the DLR Falcon aircraft and, since 2008, also on HALO [18–32].

For the ozone measurement capability, the goal was to replace one of the NIR frequency converter modules by a UV frequency converter. Since these modules have a volume of $300 \times 412 \times 256$ mm^3 the UV transmitter necessarily had to meet this footprint (see Fig. 3).

The preferred lidar transmitter for ozone DIAL should be tunable in the UV spectral range as pointed out by many

Table 1. Instrument Parameters of the Airborne Lidar

Laser	
Type	Diode pumped Nd:YAG
Energy	400 mJ at 1064 nm
Pulse duration	10 ns at 1064 nm
Repetition frequency	100 Hz
Divergence	0.5 mrad
OPO	
OPO crystals	2× KTP Type II
SFM crystal	BBO Type I
Tuning range	297–317 nm
Typical (maximum) UV output energy	10 mJ (14 mJ)
Beam diameter (expanded)	12 mm
Divergence (full angle, expanded)	<1 mrad
Spectral width	<0.044 nm (160 GHz)
Pulse duration	7 ns
Dimensions ($L \times W \times H$)	$300 \times 412 \times 256$ mm^3
Angular adjustment	Galvoscanners General Scanning Inc. M 2 ST (temp. controlled)
Wavelength Monitoring	
Fiber-coupled grating spectrometer	Ocean Optics HR4000
Receiver	
Telescope	⌀ 480 mm Cassegrain
Photomultiplier (O_3 channel)	Hamamatsu R9880U-210

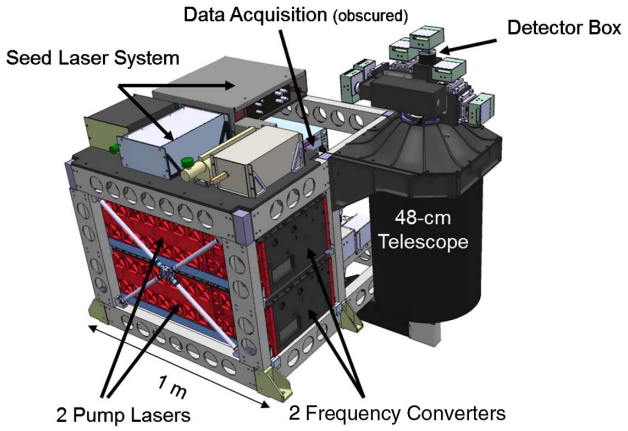

Fig. 2. Mechanical design of the WALES lidar. For the combined measurement of water vapor and ozone, one of the near-infrared frequency converters at the front end of the pump laser is exchanged against a UV frequency converter to generate the wavelengths relevant for ozone DIAL measurements.

authors (e.g., [34,35]). Tunability allows optimizing the lidar wavelengths for a selection of the optimum absorption cross sections in order to improve the signal-to-noise ratio and to optimize the measurement range, as well as to minimize interferences with other molecules and measurement errors caused by aerosol extinction and gradients [34,35].

Careful analysis suggests that the optimum on-line wavelength for ozone detection in the UTLS range is about 300–305 nm with the preferred off-line wavelength being ~10 nm longer. This is in line with other airborne ozone lidar systems developed in the past [36,37]. The envisaged accuracy and spatial resolution was 10% for 300-m vertical and 15-km horizontal averaging, respectively, as this matches with the vertical and horizontal resolution of the WALES water vapor measurement. In order to achieve this design goal it is required to generate ≈1 W of average UV power at the respective wavelengths [38].

While early UV-DIALs were based on dye laser systems [36] it is generally accepted that all-solid-state laser sources are the preferred choice for airborne operation, due to their robust and compact design. Potential, tunable solid-state laser sources are those that directly emit in the UV spectral range (such as Ce-doped lasers [39,40]) or those that emit in the visible or near IR spectral range (e.g., Ti:sapphire lasers [41] or OPOs [42–45]) whose radiation is converted into the relevant spectral range using the techniques of nonlinear frequency conversion.

Here, it was decided to use a technique that has already been used to efficiently generate tunable UV radiation starting with a Nd:YAG laser as the pump: intracavity sum frequency mixing of a near-infrared OPO [42,46]. This concept has been proven to fly on small aircraft [43,44] to measure ozone in the boundary layer. Those results, however, were obtained with pump lasers having low repetition rates of 10 Hz. One of the challenges here was to adapt this concept to the high average power of the WALES pump laser coping with higher thermal loads.

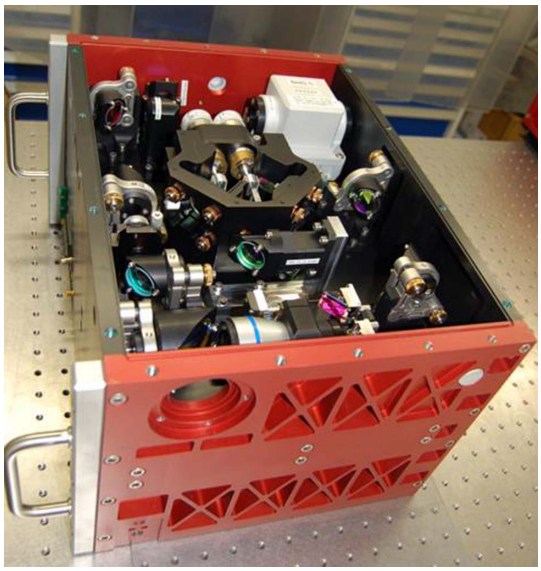

Fig. 3. Photograph of the UV frequency converter module with open cover. The upper level contains all the optics (SHG module, beam steering and conditioning, and the UV-OPO), and the lower level (obscured) comprises the temperature control for the second harmonic crystal, galvo scanner electronics, and spectrometer for wavelength control. The volume is 300 × 412 × 256 mm^3, and the weight is ~25 kg.

3. TRANSMITTER SET-UP

The UV-OPO was designed as a four-mirror ring resonator (see Fig. 4) consisting of two 12-mm long potassium titanyl phosphate (KTP) crystals cut for type-II interaction in a walk-off compensated configuration. The OPO generates signal wavelengths around 740 nm. As the pump, the second harmonic of the pump laser was generated to yield ~200 mJ of 532-nm pulse energy in a single longitudinal mode [16] at a conversion efficiency approaching 60%. The second harmonic was split into two beams by means of a dielectric beam-splitter having a split ratio of 0.625/0.375 which was found to provide the best

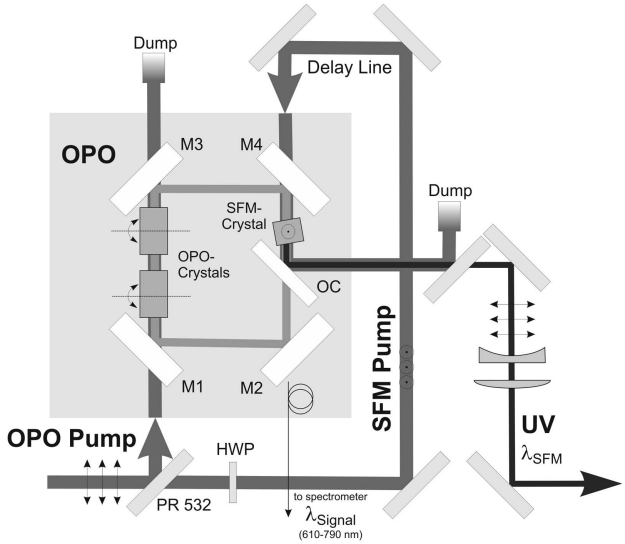

Fig. 4. Schematic set-up of the UV-OPO: M1-4, OPO cavity mirrors; PR, partial reflector; OC, outcoupling mirror; HWP, half-wave plate.

overall efficiency. The first beam serves as the pump for the OPO process, the second one is injected into the cavity to serve as the pump for the sum-frequency mixing process to take place inside the OPO cavity (see Fig. 4). The SFM-crystal is a 3-mm long β-barium borate (BBO) crystal (type I) and generates the sum frequency of the OPO signal (670–780 nm) and the 532-nm second harmonic of the Nd:YAG laser which is coupled out of the cavity using appropriate dielectric mirrors. The crystal can be that short since the intracavity process does not require a long single path interaction length [46].

All three crystals are attached to galvanometer scanners (General Scanning Inc.), and wavelength tuning is achieved by their simultaneous rotation. These drivers are controlled by the data acquisition computer of the WALES system. Since that can easily be performed at a repetition rate of 100 Hz, all wavelengths within the tuning range of this device can be addressed from pulse to pulse in an arbitrary sequence. The repeatability of the scanners is specified to be ± 15 μrad which translates into a wavelength reproducibility of <10 pm.

The continuous tuning range, within which UV energies of >1 W (10 millijoules of pulse energy) could be achieved, extended from ∼302–316 nm (Fig. 5). Therefore, also the dual-DIAL technique to minimize interferences in the presence of aerosol layers [47], can be applied as well as measuring profiles of sulfur dioxide [48,49].

The frequency converted beam is coupled out of the cavity with a dichroic mirror with high reflectivity at the UV and 532-nm wavelengths under 45 deg (see Fig. 4). Due to the nonlinear optical process the frequency converted UV radiation is well polarized. In principle, it is possible to use both UV and green radiation for the lidar. However, since green radiation is likewise generated in the water vapor module we refrain from using it here. Thus, the residual 532-nm radiation is separated from the UV and dumped. For the final beam conditioning of the UV beam, an adjustable expanding telescope is used (Qioptiq, bm.x UV2.5x) to reduce the fluence on the downstream optical components and adjust the beam divergence to ∼1 mrad.

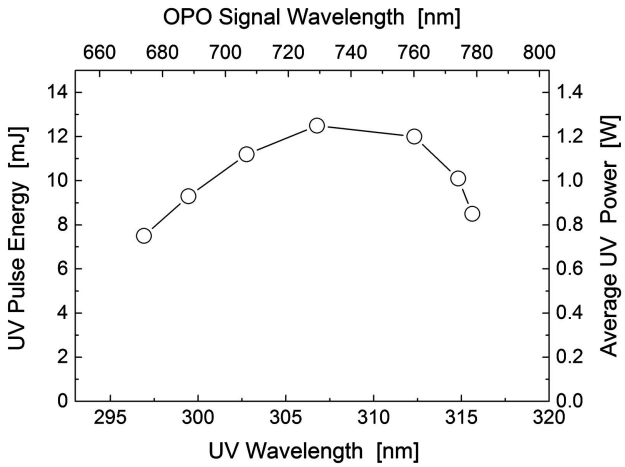

Fig. 5. Measured energy per pulse as function of wavelength in the ultraviolet spectral range and the average power (right scale), respectively. The top scale shows the corresponding OPO signal wavelength.

The maximum achieved conversion efficiency from the 1064-nm pump to the UV was as high as 4%. The bandwidth in the UV was measured to be of the order of 0.03 nm. In order to accurately monitor the wavelengths also under in-flight conditions, part of the unconverted signal radiation is transmitted to a fiber-coupled spectrometer (Ocean Optics, integrated in the lower level of the frequency converter module, see Figs. 3 and 4) optimized for the wavelength range between 610–790 nm. This spectrometer has a specified resolution of 0.11 nm in the near IR. Transferred into the UV spectral range, the wavelength precision is therefore better than 0.02 nm. During long-time measurements over more than three hours in the lab the wavelength drift was well below pixel resolution of the spectrometer. Assuming a worst case scenario that the precision is limited by the spectrometer's resolution, this transfers into a wavelength precision of 0.055 nm or an error in the determination of the ozone concentration of less than 0.4%, respectively. A comprehensive list of the transmitter parameters is given in Table 1.

4. RECEIVER SET-UP

During the experiments described below, two versions of the receiver were used. In a preliminary ground-based test the 48-cm Cassegrain telescope of the WALES system was not yet used, but a smaller one (35 cm) which has extensively been deployed for airborne lidar applications at DLR in the past including the measurements of boundary layer ozone from a small Cessna aircraft [43,44].

Due to geometrical constraints the ground-based set-up was realized as a monostatic biaxial configuration with a lateral distance between the telescope axis and laser beam of about 70 cm. Thus, a full overlap was achieved at >2 km. Since no simultaneous water vapor measurements were performed during this test, the detection system consisted of a UV–sensitive photomultiplier tube (Hamamatsu R5600) only. The solar background was suppressed using a set of four reflection filters followed by a short pass filter with a cut-off wavelength of 320 nm (SWP-320, JDSU).

The receiver system that was employed during all *airborne* measurements presented below uses the 48-cm Cassegrainian telescope of WALES [16] in a standard monostatic setup. This telescope can either be mounted in nadir- or zenith-viewing direction. The different wavelengths (1064 nm, 935 nm, 532 nm, and UV) are separated by dielectric beam-splitters. In order to make the UV measurements possible without the necessity to increase the number of detection channels, an avalanche photodiode of the cross-polarized 1064-nm channel was compromised and replaced by a UV-sensitive PMT. For the airborne version a Hamamatsu R9880U-210 PMT was used which shows a quantum efficiency of nearly 40% over the wavelength range used for ozone measurements. A dichroic with high reflectivity at $\lambda < 350$ nm and high transmission at 1064 nm now replaces the polarizing beam-splitter. Suppression of the solar background was accomplished using the above-mentioned short pass filter. The schematic set-up is depicted in Fig. 6 and a list of the transmitter parameters is given in Table 1.

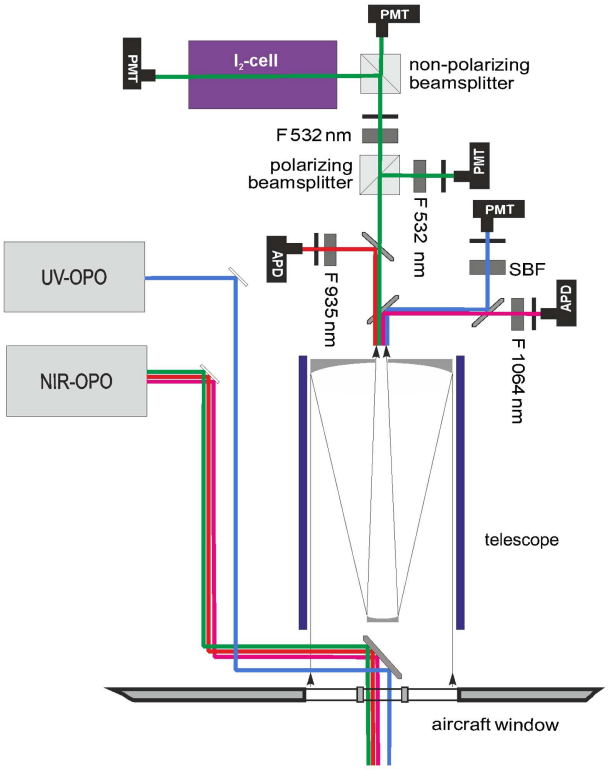

Fig. 6. Receiver layout of the combined H_2O and O_3 DIAL. The outgoing beams are transmitted behind the secondary mirror of the receiving telescope with a separation of 40 mm. The aircraft window consists of an uncoated quartz plane with a central aluminum insert that holds an antireflection coated (300–1064 nm) output window for the transmitted beams. The received beams are separated by dielectric mirrors according to their wavelength. The 532-nm channel features a depolarization channel and an iodine filter for HSRL capacity. The various channels either use photomultiplier tubes (PMT), avalanche photodiodes (APD) with suitable bandpass (F), or solar blind filters (SBF).

5. VALIDATION RESULTS

The accuracy of the water vapor channel of WALES is very well validated [16,28]. In an extensive intercomparison experiment an excellent agreement between WALES, ground-based lidars, radiosondes, and in particular a balloon-borne frost point hygrometer was demonstrated [28]. Therefore, all comparison and validation efforts within this work concentrate on the ozone channel only.

As a first test, ground-based experiments with the ozone DIAL channel in zenith-looking configuration have been performed. The ozone DIAL measurements were compared with both ozone (Brewer-Mast) sondes and ground-based lidar at the meteorological observatory of the German Weather Service (DWD) at Hohenpeissenberg which is part of the Network for the Detection of Atmospheric Composition Change (NDACC) and which is located at a distance of ~38 km from our measurement site. We found a very good agreement of the measurements (Fig. 7) that were evaluated using the ozone absorption cross sections from Daumont *et al.* [50] and Malicet *et al.* [51]. The DIAL data were averaged over 645 s and a vertical range resolution of 750 m.

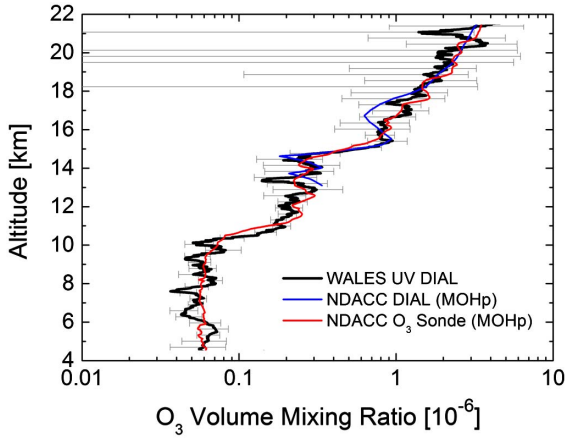

Fig. 7. Comparison of the ozone profiles measured with the UV ozone lidar to the Brewer-Mast ozonesonde and the NDACC lidar at the meteorological observatory Hohenpeissenberg (MOHp) on 20 April 2011. The tropopause level was at 10.4 km. The error bars give the statistical error of the UV DIAL measurement.

A simulation of the expected statistical error under these conditions (including the receiver configuration as described in Chapter 4) with the actual result showed an agreement within a few percent. Taking into account that the measurement geometry is very different from airborne operation where the UTLS is much closer to the lidar, we meet the expected precision indeed, which is 10% for 300 m vertical and 15 km horizontal averaging at typical aircraft velocities, respectively.

The first opportunity to operate the system onboard HALO occurred during the POLSTRACC (Polar Stratosphere in a Changing Climate) mission [52,53]. However, during that campaign the lidar worked in zenith-looking mode as one of the main objectives of the mission was the measurement of Polar Stratospheric Clouds [54] in the polar winter stratosphere. Thus, this configuration was not necessarily well suited to investigate the tropopause region. Nevertheless, during one of the flights on 21 December 2015 there was a close fly-by at the NDACC station of Ny Ålesund, Svalbard, providing an opportunity to validate the stratospheric ozone DIAL measurements with the profile from the electrochemical concentration cell (ECC) ozonesonde launched at 11:31 UT at that site. The lateral distance between aircraft and balloon was ~200 km. The results of this comparison are shown in Fig. 8. The agreement between ozonesonde and lidar is very good (bias <10%) at a range of 14.2–28 km (i.e., 1.7–15.5 km above flight level). The ozone mixing ratio is in the range of 1000–4000 ppb, i.e., much higher than at the tropopause level.

6. FIRST COMBINED H_2O AND O_3 MEASUREMENTS DURING THE WISE FIELD CAMPAIGN

During the Wave-driven Isentropic Exchange (WISE) research campaign [55] the first ever collocated DIAL nadir profile observations of H_2O and O_3 were made in the UT and LS. During WISE, a total of 17 flights with HALO were conducted from Shannon, Ireland between 13 September and 21 October

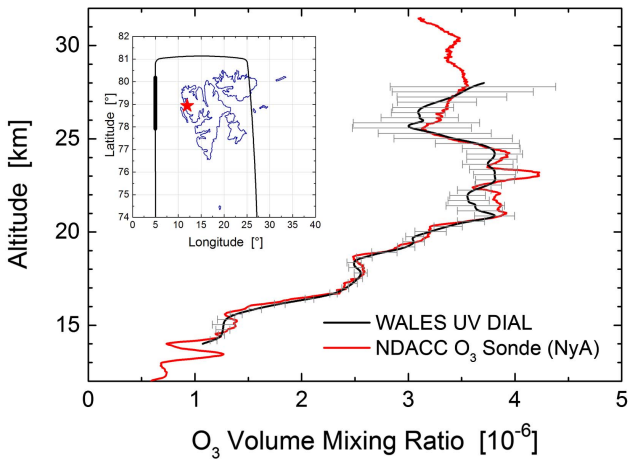

Fig. 8. Comparison of the ozone profiles measured with the UV ozone lidar to an ECC ozonesonde launched at the NDACC site of Ny Ålesund, Spitsbergen, at 11:31 UT on 21 December 2015. The black curve shows the mean of 25 profiles recorded within a circle of 200 km radius around Ny Ålesund and the error bars display the respective standard deviation. The lidar data are averaged over 80 s. The vertical range resolution is 500 m (up to 9 km above flight level), 750 m (up to 13.5 km above flight level), and 1500 m beyond. The inset shows the flight track around Svalbard and the part that was used for the comparison (thick black line).

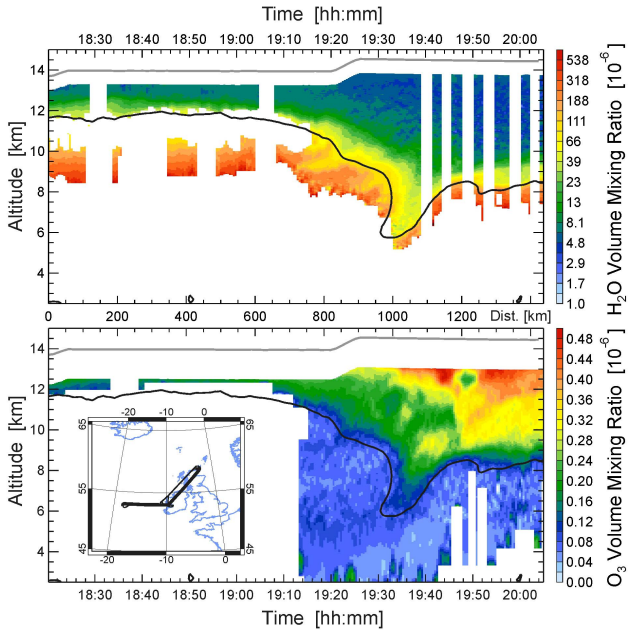

Fig. 9. DIAL observations of H_2O (top) and O_3 (bottom) mixing ratios on 28 September 2017. This ∼1.5 h flight leg (see thick black line in the inset map) covered a distance of almost 1500 km and was designed to cross a stratospheric intrusion that is clearly seen around 19:30 UT. The black curve shows the tropopause height as the 2 PVU isoline derived from ECWMF analysis. The gray line shows the flight altitude of the HALO aircraft.

2017. The scientific objective of WISE was to investigate the extratropical transition layer (ExTL) between UT and LS and in particular the transport and mixing processes related to synoptic-scale Rossby waves and their impact on the formation and composition of this layer. Flights were performed in the vicinity of the extratropical jet stream and cyclones developing over the eastern North Atlantic Ocean. The WALES instrument employed in nadir-viewing direction performed well in a number of interesting meteorological situations including several crossings of zonal jet streams and tropopause folds, multiple high-altitude observations of warm conveyor belt (WCB) outflows, and several crossings of O_3 and H_2O filaments in occluded frontal systems. Those are typical phenomena related to breaking Rossby waves leading to STE. In the context of this work, however, we restrict the analysis to an exemplary case of a single research flight in order to demonstrate the huge potential of this technique. More detailed analyses of the data recorded during the entire campaign and using the anticipated methods are beyond the scope of this paper and will be published elsewhere.

Figure 9 shows an exemplary high level flight leg from Scotland over Ireland and further west over the Atlantic Ocean performed on 28 September 2017. The case was chosen as it demonstrates the high variability of ozone and water vapor related to a variable tropopause altitude. In the first half of the flight the tropopause is located at ∼11.5 km before it folds downward between 19:30 and 19:45 UT. In the most western part of the flight the tropopause provides again a constant altitude of ∼8 km altitude. The observations show increased humidity (Fig. 9, top panel) in the troposphere. In the first half of the flight, optically thin cirrus clouds prevented observations in the first 2 km beneath the tropopause. Further west, little cloud coverage and a deep stratospheric layer increased data coverage except for some data gaps after 19:35 UT resulting from cooling issues of the H_2O channel in the low density and relatively warm stratosphere. Above the tropopause H_2O quickly decreases to very low mixing ratios in the stratosphere. O_3 shows the expected opposite behavior (Fig. 9, bottom panel); the stratosphere is dominated by high mixing ratios and smaller scale filaments. High O_3 and low H_2O mixing ratios fold downward within the stratospheric intrusion, which is a process responsible for increased transport of O_3 towards the ground [28].

Figure 10 shows the corresponding distribution of O_3 and H_2O in tracer-tracer space. The tropospheric (low O_3, high H_2O) and the stratospheric air masses (high O_3, low H_2O) are clearly separated and form linear distributions. The L-shaped distribution as shown in Fig. 1 is not completely visible, as in this particular flight in the mid-latitudes, very low tropospheric H_2O and O_3 mixing ratios that are typical of the tropical UT and LS [15] were not observed. In between tropospheric and stratospheric air masses, a zone of mixed air with an intermediate chemical characteristic is clearly visible. Mixing lines connect O_3 values of $\sim 200 \cdot 10^{-6}$ with H_2O mixing ratios of $\sim 100 \cdot 10^{-6}$.

The selected case conclusively demonstrates the inherent potential of simultaneous lidar observations of O_3 and H_2O in the tropopause region to investigate the complexity of the trace gas distribution relative to the tropopause and to study mixing and exchange processes in the UTLS. Figure 10 clearly shows a separation of transport along different mixing lines in

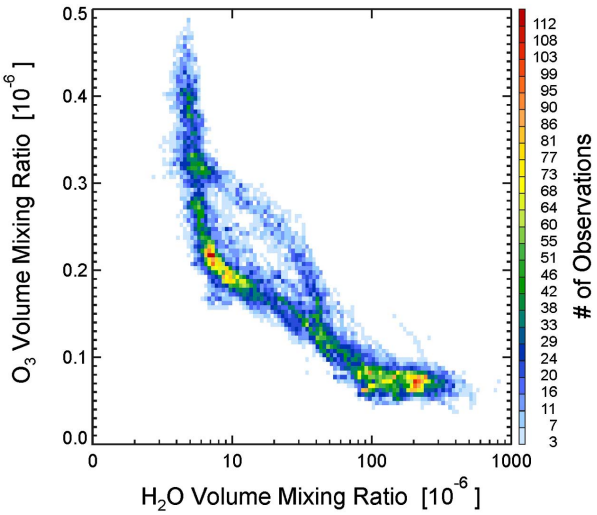

Fig. 10. Collocated DIAL observations of H_2O and O_3 in tracer-tracer space. The data are color-coded representing the frequency, giving an indication along which mixing lines the majority of the transport takes place.

tracer-tracer space which will be analyzed in more detail in the future. The data set provides much higher data coverage compared to a small number of *in situ* crossings and an opportunity for a much more detailed analysis of the relation of the dynamical and chemical transition at the tropopause.

7. CONCLUSIONS AND OUTLOOK

A new ozone lidar module has been developed that complements the existing airborne water vapor DIAL and aerosol lidar WALES and thus allows for simultaneous measurements of H_2O and O_3 profiles (and also aerosol) in the upper troposphere and lower stratosphere. This combined capability has been designed to study stratosphere-troposphere exchange by means of tracer-tracer correlation along two-dimensional curtains.

The transmitter of the ozone DIAL module is based on intracavity sum frequency mixing of the signal radiation of an OPO with 532-nm radiation from the second harmonic of a diode pumped Nd:YAG laser. This UV frequency converter has been designed in a way that it possesses the same dimensions and thus can replace one of the two near-IR frequency converters that in the original WALES set-up generates two of the four wavelengths for water vapor measurements. The UV system generates more than 10 mJ/pulse in the wavelength range of 302–317 nm at a repetition frequency of 100 Hz, i.e., >1 W of average power. The maximum overall achieved optical conversion efficiency was as high as 4%. On- and off-line wavelengths required for ozone DIAL are generated by changing the angles of the OPO and SFM crystals using galvanometer scanners to which the crystals are attached and which enable the system to generate any wavelength within the tuning range from one pulse to the next. The combined receiver set-up is designed in a way that besides the ozone and water vapor measuring capacity also aerosol backscatter and depolarization ratio as well as aerosol extinction at 532 nm using the high spectral resolution lidar technique can still be employed. Due to its tunability and bandwidth, this ozone DIAL should also be capable of applying the Dual-DIAL technique as well as measurements of sulfur dioxide profiles.

The ozone module was extensively characterized both on the ground and on aircraft and shows an excellent agreement with ozone profiles obtained with balloon-borne sondes. Finally, it was successfully demonstrated that this upgraded system is indeed capable of measuring water vapor and ozone simultaneously in the tropopause region. From this data, two-dimensional tracer-tracer plots have been retrieved which show an enormous potential to study exchange processes in the tropopause region. Based on the results of many more research flights during the WISE airborne campaign, a more detailed scientific analysis is ongoing and will be published in due course but is beyond the scope of this paper.

Acknowledgment. The Ny Ålesund ozonesonde data and the Hohenpeissenberg ozonesonde and DIAL data used in this publication were obtained from the Alfred Wegener Institute (AWI) and German Weather Service (DWD), respectively, as part of the Network for the Detection of Atmospheric Composition Change (NDACC) and are publicly available (see http://www.ndacc.org). We would like to thank Peter Hoor and Martin Riese as scientific coordinators of the WISE mission for their support.

REFERENCES

1. S. Solomon, D. Qin, M. Manning, Z. Chen, M. Marquis, K. B. Averyt, M. Tignor, and H. L. Miller, eds., *Contribution of Working Group I to the Fourth Assessment Report of the Intergovernmental Panel on Climate Change* (Cambridge University, 2007).
2. A. Maycock and A. Karpechko (lead authors), M. Abalos, H. Akiyoshi, J. M. Arblaster, C. I. Garfinkel, K. H. Rosenlof, and M. Sigmond, "Stratospheric ozone changes and climate," in *Scientific Assessment of Ozone Depletion: 2018, Global Ozone Research and Monitoring Project–Report No. 58* (World Meteorological Organization, 2018).
3. H. Fischer, F. G. Wienhold, P. Hoor, O. Bujok, C. Schiller, P. Siegmund, M. H. P. Ambaum, H. A. Scheeren, and J. Lelieveld, "Tracer correlations in the northern high latitude lowermost stratosphere: influence of cross-tropopause mass exchange," Geophys. Res. Lett. **27**, 97–100 (2000).
4. A. Zahn and C. A. M. Brenninkmeijer, "New directions: a chemical tropopause defined," Atmos. Environ. **37**, 439–440 (2003).
5. P. Hoor, C. Gurk, D. Brunner, M. I. Hegglin, H. Wernli, and H. Fischer, "Seasonality and extent of extratropical TST derived from in-situ CO measurements during SPURT," Atmos. Chem. Phys. **4**, 1427–1442 (2004).
6. L. L. Pan, W. J. Randel, B. L. Gary, M. J. Mahoney, and E. J. Hintsa, "Definitions and sharpness of the extratropical tropopause: a trace gas perspective," J. Geophys. Res. **109**, D23103 (2004).
7. G. Vaughan, C. Cambridge, L. Dean, and A. W. Phillips, "Water vapour and ozone profiles in the midlatitude upper troposphere," Atmos. Chem. Phys. **5**, 963–971 (2005).
8. H. Vogelmann and T. Trickl, "Wide-range sounding of free-tropospheric water vapor with a differential-absorption lidar (DIAL) at a high-altitude station," Appl. Opt. **47**, 2116–2132 (2008).
9. T. Trickl, H. Vogelmann, H. Giehl, H.-E. Scheel, M. Sprenger, and A. Stohl, "How stratospheric are deep stratospheric intrusions?"Atmos. Chem. Phys. **14**, 9941–9961 (2014).
10. H. Eisele, H. E. Scheel, R. Sladkovic, and T. Trickl, "High-resolution lidar measurements of stratosphere-troposphere exchange," J. Atmos. Sci. **56**, 319–330 (1999).

11. A. Papayannis, D. Balis, P. Zanis, E. Galani, H. Wernli, C. Zerefos, A. Stohl, S. Eckhardt, and V. Amiridis, "Sampling of an STT event over the Eastern Mediterranean region by lidar and electrochemical Sonde," Ann. Geophys. **23**, 2039–2050 (2005).
12. M. J. Granados-Muñoz and T. Leblanc, "Tropospheric ozone seasonal and long-term variability as seen by lidar and surface measurements at the JPL-Table Mountain Facility, California," Atmos. Chem. Phys. **16**, 9299–9319 (2016).
13. K. B. Strawbridge, M. S. Travis, B. J. Firanski, J. R. Brook, R. Staebler, and T. Leblanc, "A fully autonomous ozone, aerosol and nighttime water vapor lidar: a synergistic approach to profiling the atmosphere in the Canadian oil sands region," Atmos. Meas. Tech. **11**, 6735–6759 (2018).
14. M. I. Hegglin, C. D. Boone, G. L. Manney, T. G. Shepherd, K. A. Walker, P. F. Bernath, W. H. Daffer, P. Hoor, and C. Schiller, "Validation of ACE-FTS satellite data in the upper troposphere/lower stratosphere (UTLS) using non-coincident measurements," Atmos. Chem. Phys. **8**, 1483–1499 (2008).
15. M. I. Hegglin, C. D. Boone, G. L. Manney, and K. A. Walker, "A global view of the extratropical tropopause transition layer from atmospheric chemistry experiment Fourier transform spectrometer O3, H2O, and CO," J. Geophys. Res. **114**, D00B11 (2009).
16. M. Wirth, A. Fix, P. Mahnke, H. Schwarzer, F. Schrandt, and G. Ehret, "The airborne multiwavelength water vapor differential absorption lidar WALES: system design and performance," Appl. Phys. B **96**, 201–213 (2009).
17. M. Krautstrunk and A. Giez, "The transition from FALCON to HALO era airborne atmospheric research," in *Atmospheric Physics*, U. Schumann, ed., Research Topics in Aerospace (Springer, 2012).
18. A. Schäfler, A. Dörnbrack, C. Kiemle, S. Rahm, and M. Wirth, "Tropospheric water vapor transport as determined from airborne lidar measurements," J. Atmos. Oceanic Technol. **27**, 2017–2030 (2010).
19. C. Kiemle, M. Wirth, A. Fix, S. Rahm, U. Corsmeier, and P. Di Girolamo, "Latent heat flux measurements over complex terrain by airborne water vapour and wind lidars," Q. J. R. Meteorol. Soc. **137**, 190–203 (2011).
20. A. Schäfler, A. Dörnbrack, H. Wernli, C. Kiemle, and S. Pfahl, "Airborne lidar observations in the inflow region of a warm conveyor belt," Q. J. R. Meteorol. Soc. **137**, 1257–1272 (2011).
21. F. Harnisch, M. Weissmann, C. Cardinali, and M. Wirth, "Experimental assimilation of DIAL water vapour observations in the ECMWF global model," Q. J. R. Meteorol. Soc. **137**, 1532–1546 (2011).
22. J. S. Wagner, A. Gohm, A. Dörnbrack, and A. Schäfler, "The mesoscale structure of a polar low: airborne lidar measurements and simulations," Q. J. R. Meteorol. Soc. **137**, 1516–1531 (2011).
23. M. Wirth, "Measuring water vapor with differential absorption lidar," in *Atmospheric Physics*, U. Schumann, ed., Research Topics in Aerospace (Springer, 2012).
24. C. Kiemle, A. Schäfler, M. Wirth, A. Fix, and S. Rahm, "Detection and analysis of water vapor transport by airborne lidars," IEEE J. Sel. Top. Appl. Earth Observ. Remote Sensing **6**, 1189–1193 (2013).
25. S. Groß, M. Esselborn, F. Abicht, M. Wirth, A. Fix, and A. Minikin, "Airborne high spectral resolution lidar observation of pollution aerosol during EUCAARI-LONGREX," Atmos. Chem. Phys. **13**, 2435–2444 (2013).
26. A. Schäfler and F. Harnisch, "Impact of the inflow moisture on the evolution of a warm conveyor belt," Q. J. R. Meteorol. Soc. **141**, 299–310 (2014).
27. S. Groß, M. Wirth, A. Schäfler, A. Fix, S. Kaufmann, and C. Voigt, "Potential of airborne lidar measurements for cirrus cloud studies," Atmos. Meas. Tech. **7**, 2745–2755 (2014).
28. T. Trickl, H. Vogelmann, A. Fix, A. Schäfler, M. Wirth, B. Calpini, G. Levrat, G. Romanens, A. Apituley, K. M. Wilson, R. Begbie, J. Reichardt, H. Vömel, and M. Sprenger, "How stratospheric are deep stratospheric intrusions?–LUAMI 2008," Atmos. Chem. Phys. **16**, 8791–8815 (2016).
29. C. Kiemle, S. Groß, M. Wirth, and L. Bugliaro, "Airborne lidar observations of water vapor variability in tropical shallow convective environment," in *Shallow Clouds, Water Vapor, Circulation, and Climate Sensitivity*, R. Pincus, D. Winker, S. Bony, and B. Stevens, eds., Space Sciences Series of ISSI (Springer, 2017), Vol. 65.
30. C. Voigt, U. Schumann, A. Minikin, A. Abdelmonem, A. Afchine, S. Borrmann, M. Boettcher, B. Buchholz, L. Bugliaro, A. Costa, J. Curtius, M. Dollner, A. Dörnbrack, V. Dreiling, V. Ebert, A. Ehrlich, A. Fix, L. Forster, F. Frank, D. Fütterer, A. Giez, K. Graf, J. Grooß, S. Groß, K. Heimerl, B. Heinold, T. Hüneke, E. Järvinen, T. Jurkat, S. Kaufmann, M. Kenntner, M. Klingebiel, T. Klimach, R. Kohl, M. Krämer, T. C. Krisna, A. Luebke, B. Mayer, S. Mertes, S. Molleker, A. Petzold, K. Pfeilsticker, M. Port, M. Rapp, P. Reutter, C. Rolf, D. Rose, D. Sauer, A. Schäfler, R. Schlage, M. Schnaiter, J. Schneider, N. Spelten, P. Spichtinger, P. Stock, A. Walser, R. Weigel, B. Weinzierl, M. Wendisch, F. Werner, H. Wernli, M. Wirth, A. Zahn, H. Ziereis, and M. Zöger, "ML-CIRRUS: the airborne experiment on natural cirrus and contrail cirrus with the high-altitude long-range research aircraft HALO," Bull. Amer. Meteor. Soc. **98**, 271–288 (2017).
31. B. Urbanek, S. Groß, A. Schäfler, and M. Wirth, "Determining stages of cirrus evolution: a cloud classification scheme," Atmos. Meas. Tech. **10**, 1653–1664 (2017).
32. A. Schäfler, G. Craig, H. Wernli, P. Arbogast, J. D. Doyle, R. McTaggart-Cowan, J. Methven, G. Rivière, F. Ament, M. Boettcher, M. Bramberger, Q. Cazenave, R. Cotton, S. Crewell, J. Delanoë, A. Dörnbrack, A. Ehrlich, F. Ewald, A. Fix, C. M. Grams, S. L. Gray, H. Grob, S. Groß, M. Hagen, B. Harvey, L. Hirsch, M. Jacob, T. Kölling, H. Konow, C. Lemmerz, O. Lux, L. Magnusson, B. Mayer, M. Mech, R. Moore, J. Pelon, J. Quinting, S. Rahm, M. Rapp, M. Rautenhaus, O. Reitebuch, C. A. Reynolds, H. Sodemann, T. Spengler, G. Vaughan, M. Wendisch, M. Wirth, B. Witschas, K. Wolf, and T. Zinner, "The North Atlantic waveguide and downstream impact experiment," Bull. Amer. Meteor. Soc. **99**, 1607–1637 (2018).
33. T. Trickl, H. Vogelmann, H. Flentje, and L. Ries, "Stratospheric ozone in boreal fire plumes–the 2013 smoke season over central Europe," Atmos. Chem. Phys. **15**, 9631–9649 (2015).
34. J. Pelon and G. Mégie, "Ozone monitoring in the troposphere and lower stratosphere: evaluation and operation of a ground-based lidar station," J. Geophys. Res. **87**, 4947–4955 (1982).
35. M. H. Proffitt and A. O. Langford, "Ground-based differential absorption lidar system for day or night measurements of ozone throughout the free troposphere," Appl. Opt. **36**, 2568–2585 (1997).
36. E. V. Browell, S. Ismail, and W. Grant, "Differential absorption lidar (DIAL) measurements from air and space," Appl. Phys. B **67**, 399–410 (1998).
37. G. Ancellet and F. Ravetta, "Compact airborne lidar for tropospheric ozone: description and field measurements," Appl. Opt. **37**, 5509–5521 (1998).
38. F. Steinebach, "Entwicklung, Charakterisierung und Anwendung eines durchstimmbaren Lidartransmitters im ultravioletten Spektralbereich für die Vermessung von Ozon in der Tropopausenregion," Ph.D. thesis (LMU München, 2012).
39. R. J. Alvarez, C. J. Senff, A. O. Langford, A. M. Weickmann, D. C. Law, J. L. Machol, D. A. Merritt, R. D. Marchbanks, S. P. Sandberg, W. A. Brewer, R. M. Hardesty, and R. M. Banta, "Development and application of a compact, tunable, solid-state airborne ozone lidar system for boundary layer profiling," J. Atmos. Oceanic Technol. **28**, 1258–1272 (2011).
40. R. De Young, W. Carrion, R. Ganoe, D. Pliutau, G. Gronoff, T. Berkoff, and S. Kuang, "Langley mobile ozone lidar: ozone and aerosol atmospheric profiling for air quality research," Appl. Opt. **56**, 721–730 (2017).
41. K. A. Elsayed, S. Chen, L. B. Petway, B. L. Meadows, W. D. Marsh, W. C. Edwards, J. C. Barnes, and R. J. DeYoung, "High-energy, efficient, 30-Hz ultraviolet laser sources for airborne ozone-lidar systems," Appl. Opt. **41**, 2734–2739 (2002).
42. A. Fix, M. Wirth, A. Meister, G. Ehret, M. Pesch, and D. Weidauer, "Tunable ultraviolet optical parametric oscillator for differential absorption lidar measurements of tropospheric ozone," Appl. Phys. B **75**, 153–163 (2002).
43. A. Meister, "Entwicklung eines UV-Lasertransmitters und Aufbau eines flugzeuggetragenen DIAL für Ozonmessungen in der Troposphäre," Ph. D. thesis (University of Bayreuth, 2005).
44. A. Meister, A. Fix, H. Flentje, M. Wirth, and G. Ehret, "TropOLEX: a new tuneable airborne lidar system for the measurement of

tropospheric ozone," in *6th International Symposium on Tropospheric Profiling*, Leipzig, Germany, 14–20 September 2003, pp. 233–253.
45. J. W. Hair, C. Cleckner, K. Murray, D. Fratello, C. Naftel, J. Collins, A. Notari, and W. Welch, "Development of the Global Ozone Lidar Demonstrator (GOLD) for the Global Hawk," available at https://esto.nasa.gov/conferences/estf2010/papers/Hair_ESTF2010.pdf (NASA Langley Research Center, 2010).
46. A. Fix and G. Ehret, "Intracavity frequency mixing in pulsed optical parametric oscillators for the efficient generation of continuously tunable ultraviolet radiation," Appl. Phys. B **67**, 331–338 (1998).
47. Z. Wang, H. Nakane, H. Hu, and J. Zhou, "Three-wavelength dual differential absorption lidar method for stratospheric ozone measurements in the presence of volcanic aerosols," Appl. Opt. **36**, 1245–1252 (1997).
48. T. Fujii, T. Fukuchi, N. Goto, K. Nemoto, and N. Takeuchi, "Dual differential absorption lidar for the measurement of atmospheric SO2 of the order of parts in 10^9," Appl. Opt. **40**, 949–956 (2001).
49. T. Fujii, T. Fukuchi, N. Cao, K. Nemoto, and N. Takeuchi, "Trace atmospheric SO2 measurement by multiwavelength curve-fitting and wavelength-optimized dual differential absorption lidar," Appl. Opt. **41**, 524–531 (2002).
50. D. Daumont, J. Brion, J. Charbronnier, and J. Malicet, "Ozone UV spectroscopy I: Absorption cross section at room temperature II: Absorption cross sections and temperature dependence," J. Atmos. Chem. **15**, 145–155 (1992).
51. J. Malicet, D. Daumont, J. Charbronnier, C. Parisse, A. Chakir, and J. Brion, "Ozone UV spectroscopy. II. Absorption cross-sections and temperature dependence," J. Atmos. Chem. **21**, 263–273 (1995).
52. H. Oelhaf, B. M. Sinnhuber, W. Woiwode, M. Rapp, A. Dörnbrack, A. Engel, and H. Bönisch, "The polar stratosphere in a changing climate (POLSTRACC): mission overview and first results," in *EGU General Assembly Conference Abstracts* (2016), Vol. **18**, p. 7743.
53. H. Oelhaf, B.-M. Sinnhuber, W. Woiwode, H. Bönisch, H. Bozem, A. Engel, A. Fix, F. Friedl-Vallon, J.-U. Grooß, P. Hoor, S. Johansson, T. Jurkat-Witschas, S. Kaufmann, M. Krämer, J. Krause, E. Kretschmer, D. Lörks, A. Marsing, J. Orphal, K. Pfeilsticker, M. Pitss, L. Poole, P. Preusse, M. Rapp, M. Riese, C. Rolf, J. Ungermann, C. Voigt, C. M. Volk, M. Wirth, A. Zahn, and H. Ziereis, "POLSTRACC: airborne experiment for studying the polar stratosphere in a changing climate with the high-altitude long-range research aircraft HALO," Bull. Amer. Meteor. Soc., submitted for publication.
54. C. Voigt, A. Dörnbrack, M. Wirth, S. M. Groß, M. C. Pitts, L. R. Poole, R. Baumann, B. Ehard, B.-M. Sinnhuber, W. Woiwode, and H. Oelhaf, "Widespread polar stratospheric ice clouds in the 2015–2016 Arctic winter–implications for ice nucleation," Atmos. Chem. Phys. **18**, 15623–15641 (2018).
55. M. Riese, P. Hoor, D. Kunkel, and M. Kaufmann, "The wave-driven isentropic exchange (WISE) mission: campaign overview and first results," in *EGU General Assembly Conference Abstracts* (2018), Vol. **20**, p. 18980.